

SUPPORTING INFORMATION

High-Efficiency “Working-in-Tandem” Nitrogen Photofixation Achieved by Assembling Plasmonic Gold Nanocrystals on Ultrathin Titania Nanosheets

Jianhua Yang,[†] Yanzhen Guo,[†] Ruibin Jiang,^{*,‡} Feng Qin,[†] Han Zhang,[†] Wenzheng Lu,[†] Jianfang Wang,^{*,†} and Jimmy C. Yu[§]

[†]Department of Physics, The Chinese University of Hong Kong, Shatin, Hong Kong SAR, China

[‡]Shaanxi Key Laboratory for Advanced Energy Devices, Shaanxi Engineering Lab for Advanced Energy Technology, School of Materials Science and Engineering, Shaanxi Normal University, Xi'an 710119, China

[§]Department of Chemistry, The Chinese University of Hong Kong, Shatin, Hong Kong SAR, China

Supporting Text

Characterization

X-ray diffraction (XRD) patterns were acquired on a Rigaku SmartLab diffractometer equipped with Cu K α radiation. Atomic force microscopy (AFM) imaging was performed in air on a Veeco Metrology system (model No. 920-006-101) that was operated at the contact mode using a super-sharp Si₃N₄ tip (Nanoprobes). Scanning electron microscopy (SEM) images were taken on an FEI Quanta 400 FEG microscope. Transmission electron microscopy (TEM) imaging was performed on an FEI Tecnai Spirit microscope operated at 120 kV. High-resolution TEM (HRTEM), high-angle annular dark-field scanning transmission electron microscopy (HAADF-STEM) imaging and elemental mapping were carried out on an FEI Tecnai F20 microscope equipped with an Oxford energy-dispersive X-ray analysis system. The extinction spectra of the Au nanocrystal samples, the absorption spectra for the determination of ammonia and the absorption spectra of the powder samples were measured on an ultraviolet/visible/near-infrared

spectrophotometer (PerkinElmer Lambda 950). N₂ adsorption-desorption isotherms were measured on a Micromeritics Tristar II 3020 system. Low-temperature electron paramagnetic resonance (EPR) spectra were acquired on a Bruker EMX EPR spectrometer (Billerica, MA) at 77 K. X-ray photoelectron spectroscopy (XPS) measurements were performed on a PerkinElmer PHI 5000C system, with all binding energies calibrated using contaminant carbon (C 1s at 284.6 eV) as a reference. N₂ temperature-programmed desorption (TPD) analysis was performed in a quartz reactor using a thermal conductivity detector. Briefly, 0.25 g of the catalyst was first pre-treated with pure He at a flow rate of 50 mL·min⁻¹ at 120 °C for 30 min, followed by cooling down to room temperature in the same atmosphere and then dosed with pure N₂. To remove residual N₂, the catalyst was purged with pure He at a flow rate of 50 mL·min⁻¹ for 30 min. The N₂ TPD measurement was subsequently performed up to 350 °C at a heating rate of 5 °C·min⁻¹ in pure He. Fourier transform infrared spectroscopy (FTIR) was performed on a Thermo Nicolet NEXUS 670 spectrometer. *In situ* diffuse-reflectance infrared Fourier transform spectroscopy (DRIFTS) was conducted on a Nicolet iS50 FT-IR spectrometer with a home-designed reaction cell. The catalyst (80 mg) was pressed at 25 Mpa for 0.5 h to make a round pellet of 0.35 cm in radius and ~0.5 mm in thickness. The catalyst pellet was placed at the center in the reaction cell, followed by pumping out all gases in the reaction cell with an ultrahigh vacuum pump. The reaction cell was purged with dry Ar for 15 min. A mixture of H₂O vapor and N₂ (or Ar) at the concentration of ~0.06 g H₂O per liter of N₂ (or Ar) at a flow rate of 50 mL/min was pumped into the reaction cell in order to form a moist atmosphere and a thin layer of water on the catalyst surface. The H₂O vapor was generated using a household ultrasonic humidifier (1.7 MHz, 30 W). It was mixed with and carried by N₂ (or Ar) flow using a Y-shaped tube. After 30-min pretreatment, the visible light was turned on and the infrared signal at a resolution of 2 cm⁻¹ for 32 scans was *in situ* collected. The background spectrum was collected beforehand and subtracted from the recorded spectra automatically. Thermogravimetric analysis (TGA) was conducted on a Perkin Elmer TGA 6 thermogravimetric analyzer. The heating rate was 10 °C·min⁻¹. Steady-state surface photovoltage (SPV) measurements were carried out in an integrated system including a source of monochromatic light, a lock-in amplifier (SR830-DSP) with a light chopper (SR540) and a photovoltaic cell. The monochromatic light source was generated from a 500-W Xe lamp in conjunction with a double-prism monochromator. For transient absorption spectroscopy (TAS), 1.2 mg of the catalyst sample was suspended in a

mixture solution of acetonitrile (2.5 mL), water (2.25 mL) and methanol (0.25 mL) through sonication. The resultant suspension was bubbled with continuous Ar flow for 40 min to remove dissolved air. Before the measurement, Ar or N₂ stream was flowed into the cell for 20 min. The excitation source was a 532-nm laser (45 mJ, pulse ≤ 7 ns). The transient signal was obtained with a Tektronix 2440 digitizer. The Au atomic ratios in the catalyst samples were determined by inductively coupled plasma mass spectrometry (ICP-MS, Agilent). Before the ICP-MS measurement, the Au nanocrystals in the catalyst samples were dissolved by *aqua regia* to Au³⁺ ions. The linear calibration curve of Au³⁺ was obtained from HAuCl₄ solutions of known concentrations.

Supporting Figures

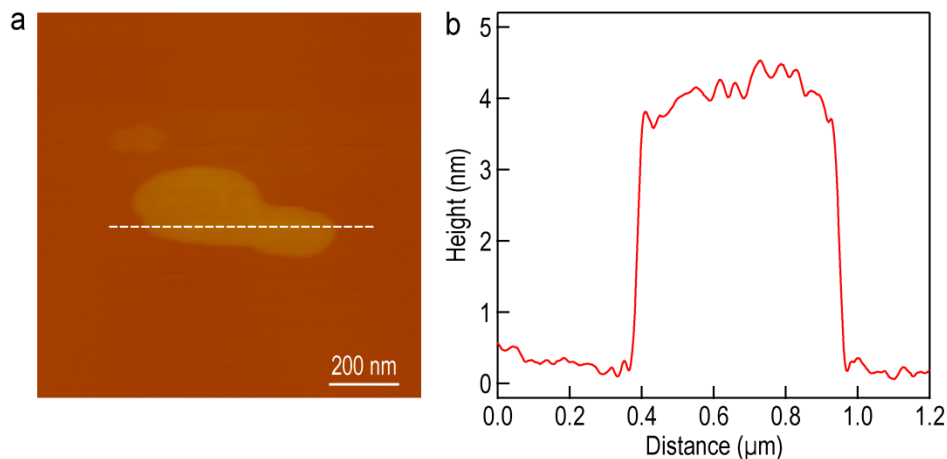


Figure S1. AFM characterization. (a) AFM image of the as-prepared TiO₂-OV nanosheets. (b) Height profile extracted along the solid line indicated in (a).

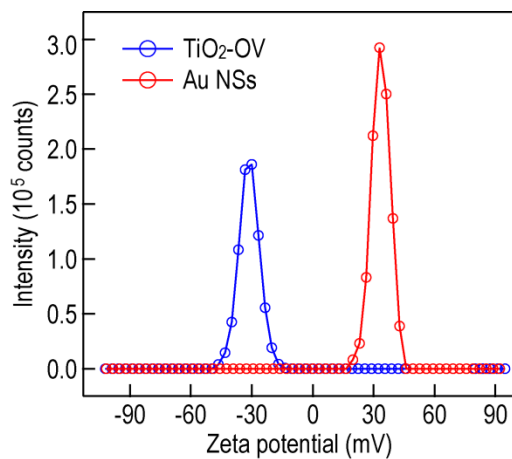


Figure S2. Zeta potential measurements. Zeta potentials of the Au nanospheres (Au NSs) and the TiO₂-OV nanosheets dispersed in water.

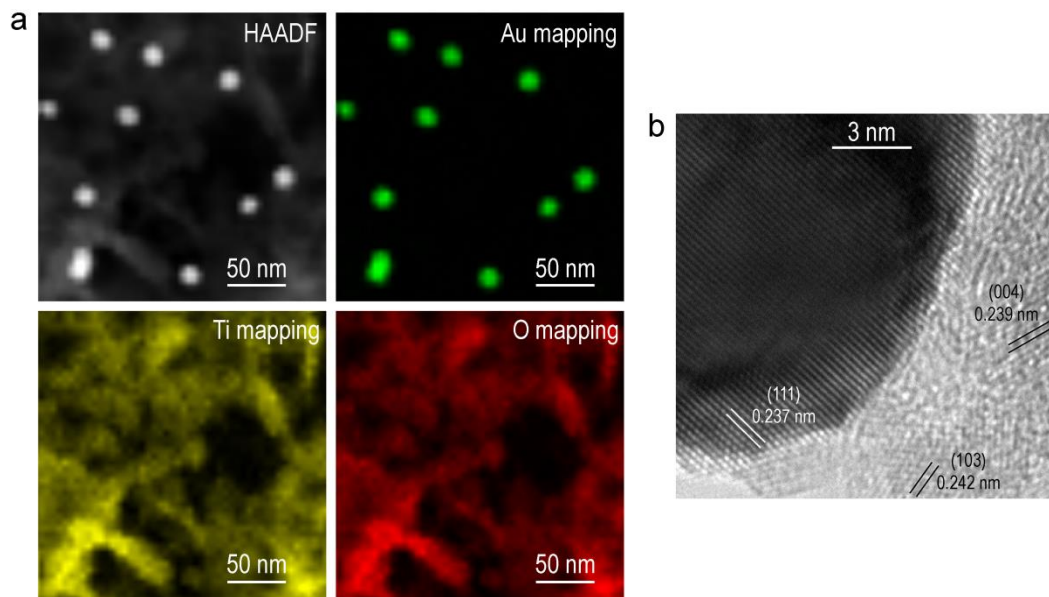


Figure S3. TEM characterization. (a) HAADF-STEM image, elemental maps of Au, Ti and O of the Au/TiO₂-OV sample. (b) HRTEM image of the Au/TiO₂-OV sample, showing the lattice fringes of Au and TiO₂.

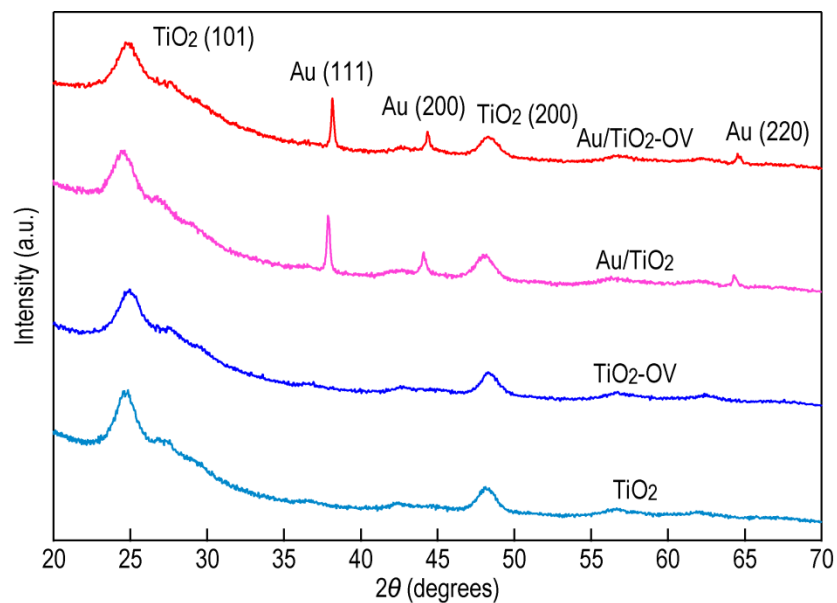


Figure S4. XRD characterization. XRD patterns of the Au/TiO₂-OV, Au/TiO₂, TiO₂-OV and TiO₂ samples. The diffraction peaks can be indexed according to the face-centered-cubic Au phase (JCPDS #: 01-1172) and the tetragonal anatase TiO₂ phase (JCPDS #: 04-0477). According to the (200) diffraction peak of TiO₂, the lattice constant b is estimated to be 0.38 nm.

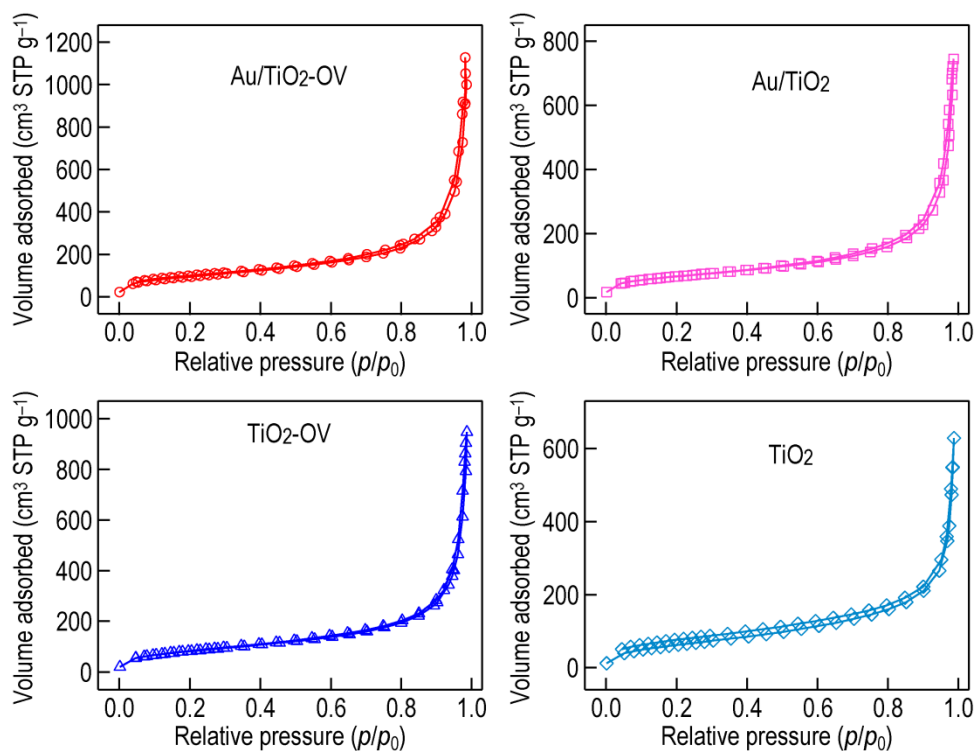


Figure S5. N₂ adsorption-desorption isotherms. All of the four samples were measured. Their specific surface areas are listed in Table S1.

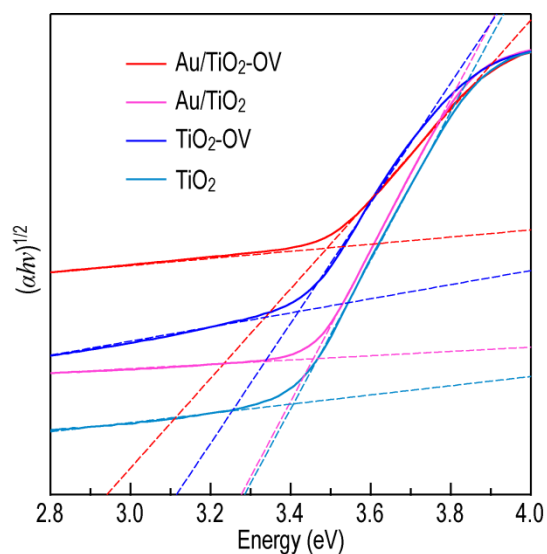


Figure S6. Tauc plots of the four catalysts. The curves were converted from the absorption spectra shown in Figure 1f and plotted in the range from 2.8 eV to 4.0 eV.

The electronic bandgap was calculated using the Tauc relation,¹ which is given as

$$\alpha h\nu = B(h\nu - E_g)^n$$

where $h\nu$ is the incident photon energy, B is a constant, E_g is the bandgap to be determined, and n is a constant. n is 1/2 for semiconductors with direct bandgaps and 2 for semiconductors with indirect bandgaps. The anatase phase of TiO_2 has an indirect bandgap.² Therefore n is 2. The parameter, α , represents the absorption coefficient. It depends on the measured light absorption, A (in percentage), and the sample thickness, d , as given in the following equation

$$\alpha = \frac{1}{d} \ln \left[\frac{1}{1 - (A/100)} \right]$$

In our experiments, $d = 2$ mm. The plots of $(\alpha h\nu)^{1/2}$ against $h\nu$ are shown in Figure S6. The electronic bandgap of each sample was determined from the intersection of the straight-line extrapolations above and below the knee energy point.

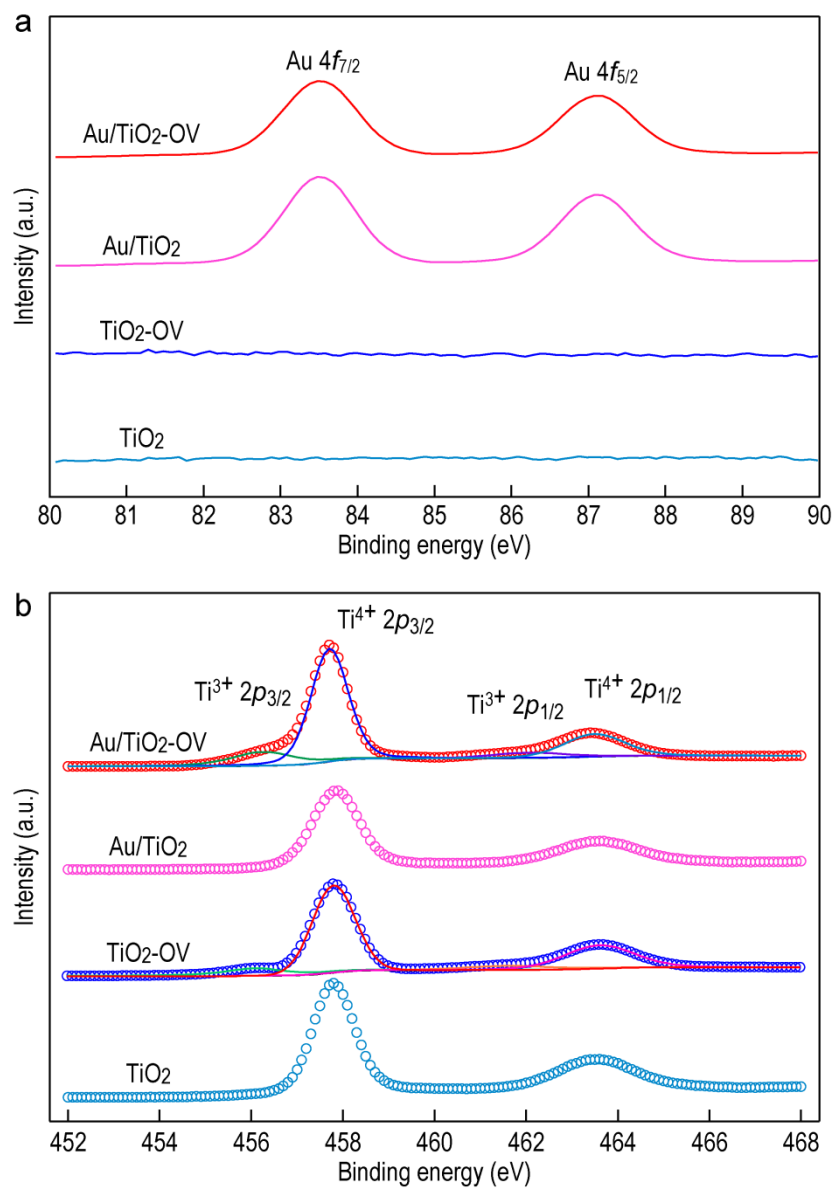


Figure S7. XPS characterization. (a) High-resolution Au 4f XPS spectra of the catalyst samples. (b) High-resolution Ti 2p XPS spectra of the catalyst samples.

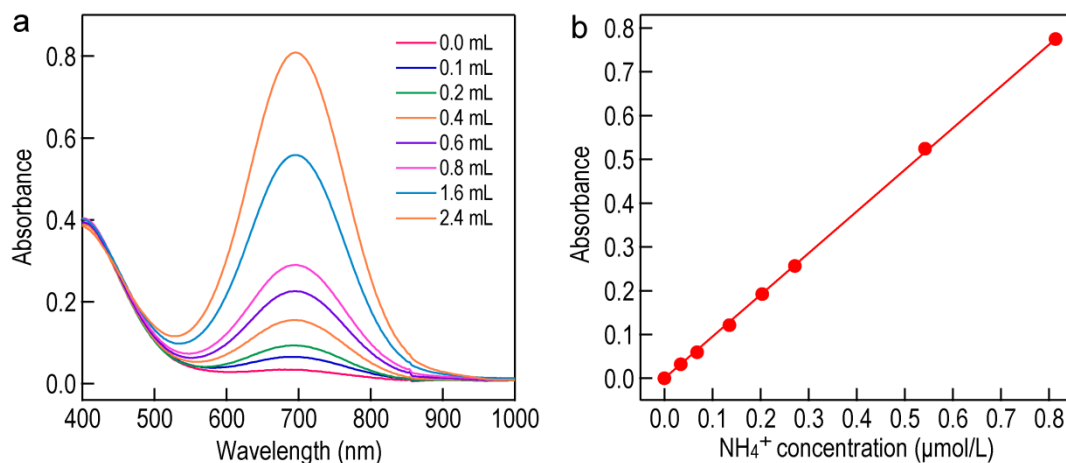


Figure S8. Calibration for NH_4^+ determination. (a) Absorption spectra of the testing solutions containing NH_4^+ at different concentrations. (b) Linear relationship between the peak absorbance at 697 nm and the NH_4^+ concentration.

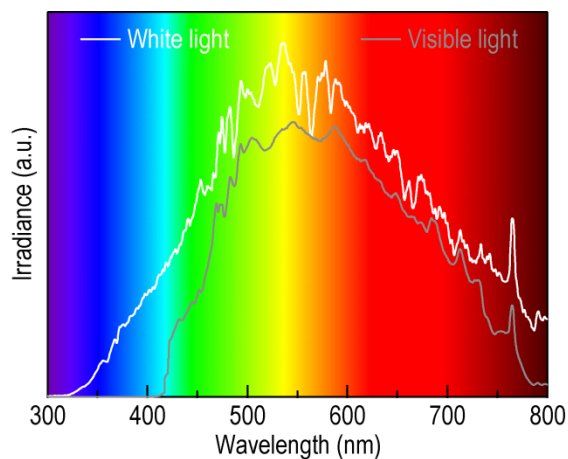


Figure S9. Excitation light sources. Emission spectra of the Xe lamp (white light) and the Xe lamp equipped with a 420-nm cut-off filter (visible light).

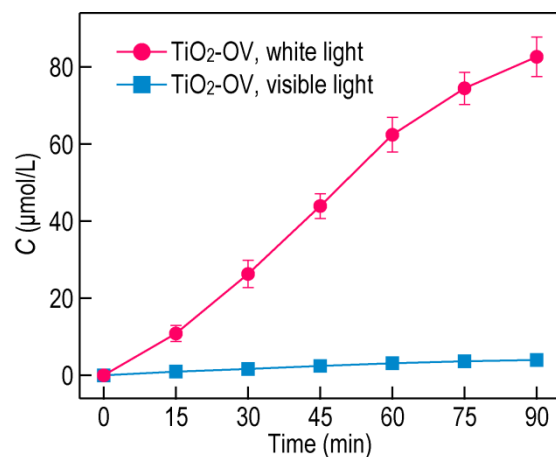


Figure S10. Nitrogen photofixation with the TiO₂-OV sample. The ammonia concentrations were plotted as functions of the irradiation time under the white and visible light, respectively.

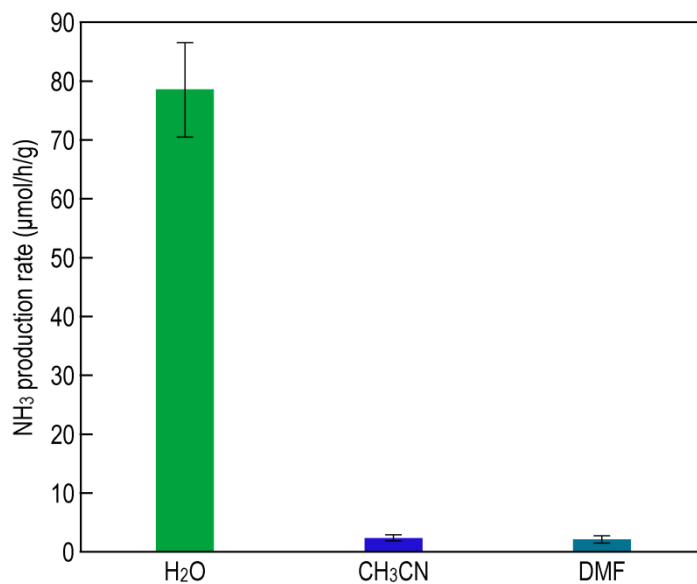


Figure S11. N₂ photofixation in different solvents. The NH₃ production rates with the Au/TiO₂-OV sample in different solvents under the visible light are shown. DMF represents dimethylformamide.

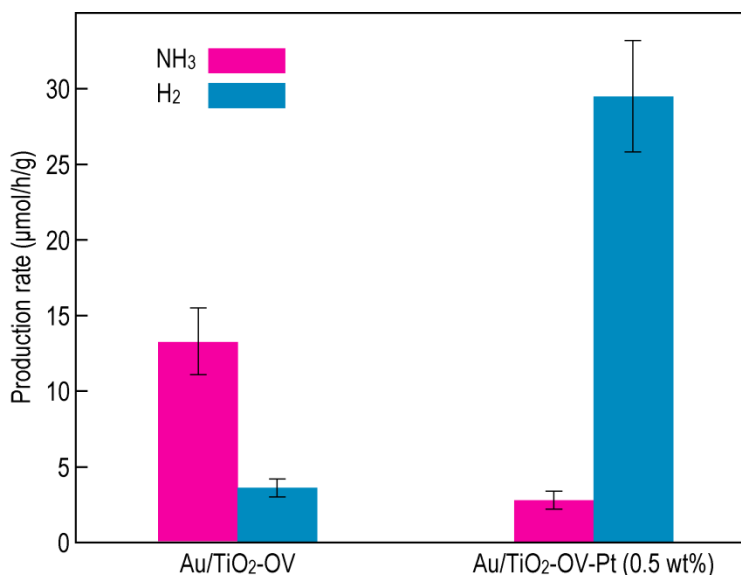


Figure S12. H₂ co-evolution. The production rates of NH₃ and H₂ during the N₂ photofixation with the Au/TiO₂-OV and Au/TiO₂-OV-Pt samples in a sealed reactor are shown. The N₂ photofixation reaction and the H₂ evolution reaction are competitive. Loading Pt can boost the H₂ production, while the ammonia evolution is greatly inhibited, suggesting the competition between the two reactions. The competition between N₂ photofixation and H₂ evolution represents an interesting yet challenging topic in photochemical field.

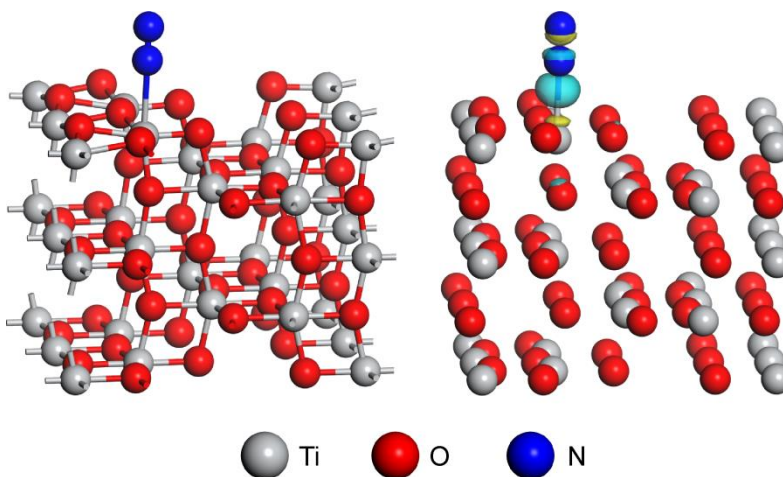


Figure S13. N₂ chemisorption on the OV-free TiO₂ surface. Adsorption configuration (left) and charge density difference (right) of a N₂ molecule adsorbed on the OV-free TiO₂ surface. The light blue and yellow isosurfaces represent charge accumulation and depletion in space, respectively. The isovalue is 0.01 e Å⁻³.

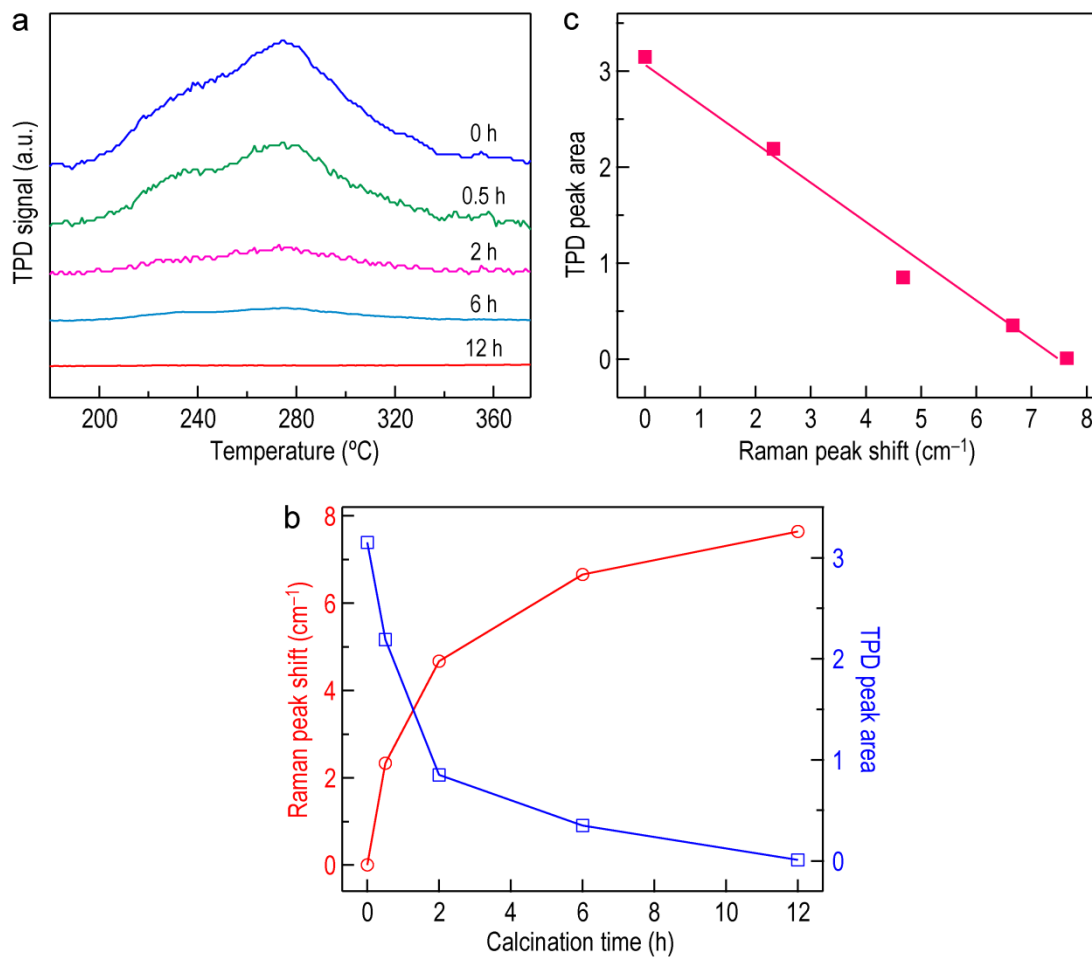


Figure S14. Control of the OV concentration. (a) N₂ TPD profiles of the Au/TiO₂-OV sample that was calcined in air for different periods of time. (b) Raman peak shifts (left axis) and integrated TPD peak areas (right axis) as functions of the calcination time. (c) Linear variation of the integrated TPD peak area with the Raman peak shift.

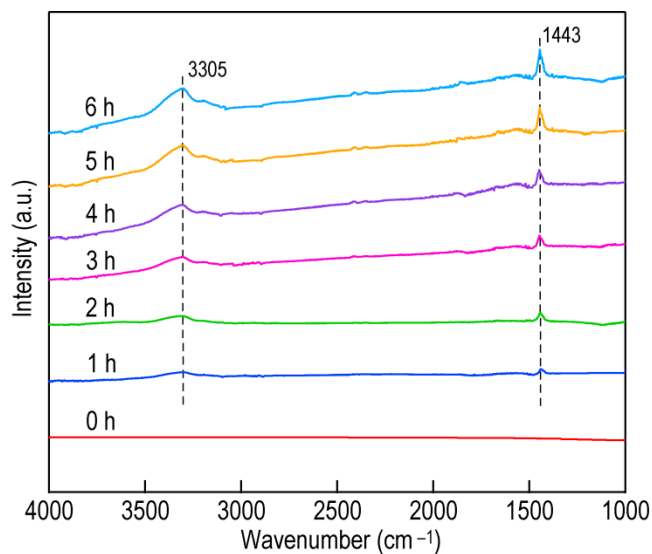


Figure S15. *In situ* DRIFTS spectra recorded as a function of time on the Au/TiO₂-OV catalyst in Ar atmosphere. The numbers indicate the wavenumbers of the different vibrational modes.

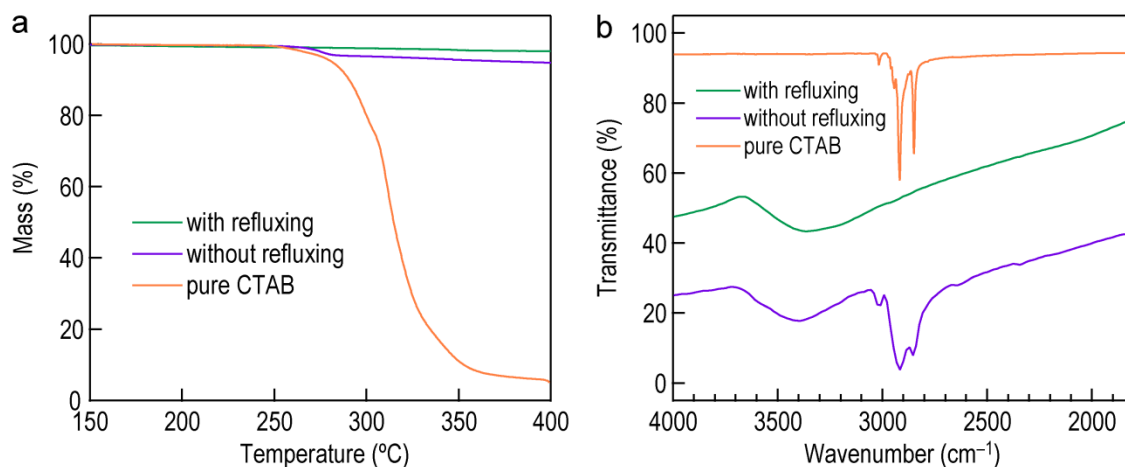


Figure S16. Effect of refluxing in acetone. (a) TGA traces of the Au/TiO₂-OV sample with the refluxing treatment, the Au/TiO₂-OV sample without the refluxing treatment, and pure CTAB. (b) FTIR spectra of the same three samples.

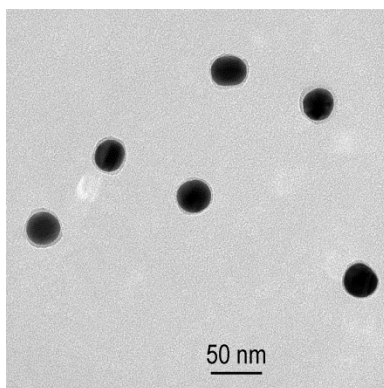


Figure S17. (Au core)@(SiO₂ shell) nanostructures. TEM image of the core@shell nanostructures for the preparation of Au@SiO₂/TiO₂-OV. The SiO₂ shell is 2.1 ± 0.2 nm in thickness.

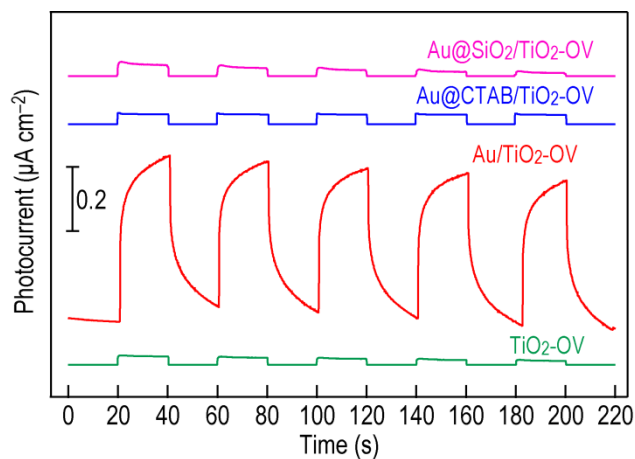


Figure S18. Photocurrent measurements. The photocurrents were measured for the Au@SiO₂/TiO₂-OV, Au@CTAB/TiO₂-OV, Au/TiO₂-OV and TiO₂-OV samples with the visible light irradiation switched on and off repeatedly.

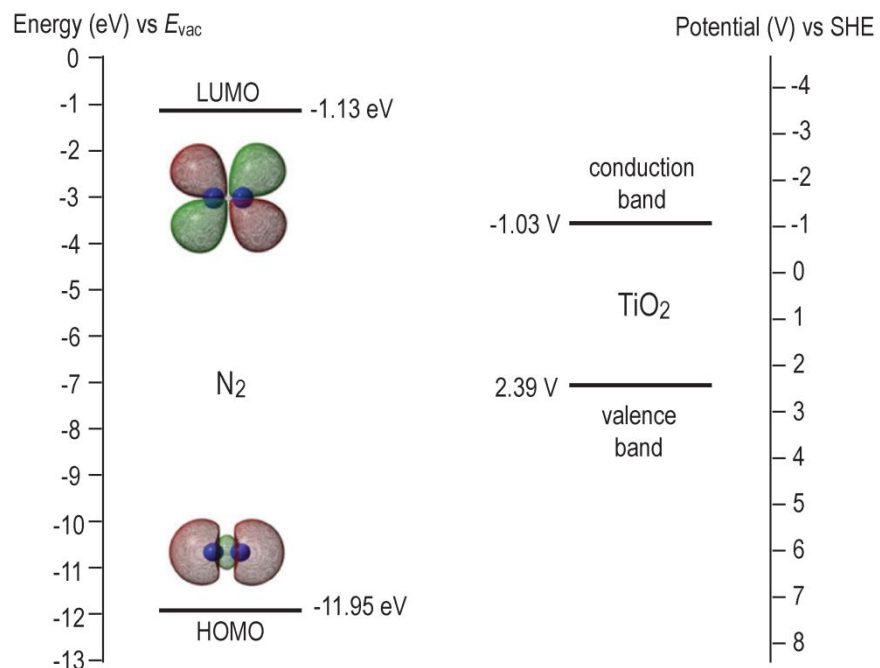


Figure S19. LUMO and HOMO energy levels of free N₂ molecules and the conduction and valence band edges of TiO₂.

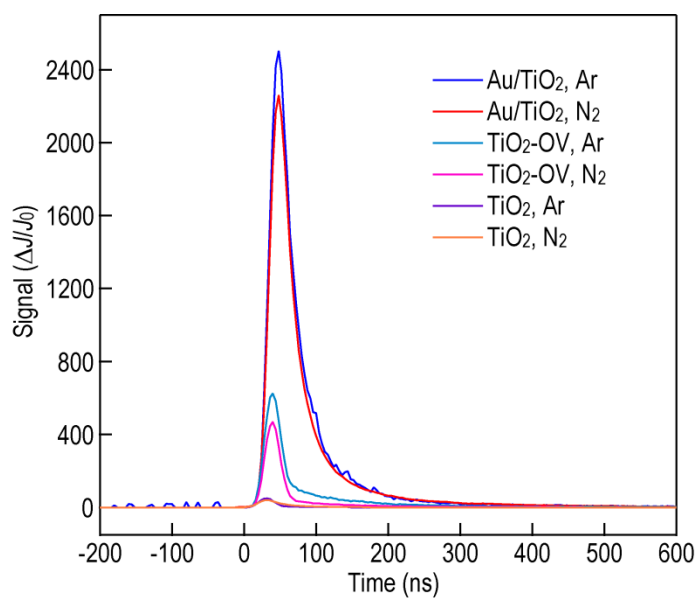


Figure S20. Transient absorption spectra. The spectra were measured on the TiO₂, TiO₂-OV and Au/TiO₂ samples under inert (Ar) and reactive (N₂) atmosphere, respectively.

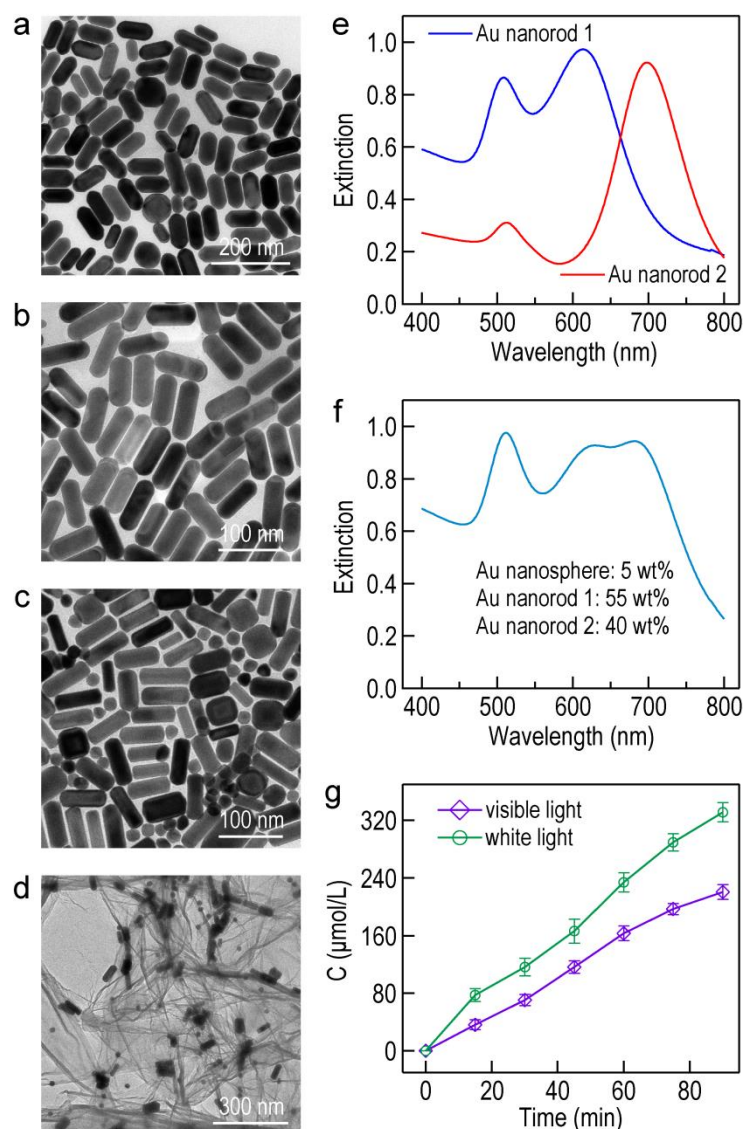


Figure S21. Further improvement of the N₂ photofixation activity. (a) TEM image of the Au nanorod sample (Au nanorod 1, 88 ± 10 nm in length and 43 ± 3 nm in diameter, length-to-diameter aspect ratio 2.2 ± 0.2) with the longitudinal plasmon wavelength at 615 nm. (b) TEM image of the Au nanorod sample (Au nanorod 2, 85 ± 8 nm in length and 29 ± 2 nm in diameter, length-to-diameter aspect ratio 2.9 ± 0.3) with the longitudinal plasmon wavelength at 697 nm. (c) TEM image of the mixture of the Au nanosphere sample and the two Au nanorod samples. (d) TEM image of the mixed Au nanocrystals attached on the TiO₂-OV nanosheets. (e) Extinction spectra of the two Au nanorod samples. (f) Extinction spectrum of the Au nanocrystal mixture. (g) Concentrations of ammonia produced with the Au mixture/TiO₂-OV sample under the visible and white light, respectively.

To enhance the light absorption at visible wavelengths, the Au mixture/TiO₂-OV sample was prepared. The Au nanosphere sample was mixed together with two Au nanorod samples. The Au nanosphere sample has a plasmon peak at 520 nm in aqueous solutions. The longitudinal and transverse plasmon peaks of one Au nanorod sample are at 615 and 508 nm, and those of the other Au nanorod sample are at 697 and 513 nm, respectively. The Au nanocrystal mixture solution was produced by adding the Au nanorod 1 solution (4.05 mL, extinction spectrum shown in Figure S21e) and the Au nanorod 2 solution (5.15 mL, extinction spectrum shown in Figure S19e) in the Au nanosphere solution (0.80 mL, extinction spectrum shown in Figure 1c). The mixture of the Au nanocrystals exhibits large extinction over the visible range.

Supporting Tables

Table S1. Specific Surface Areas and Electronic Bandgaps of the Catalysts

catalyst	specific surface area (m ² g ⁻¹)	electronic bandgap (eV)
Au/TiO ₂ -OV	288	3.48
Au/TiO ₂	237	3.45
TiO ₂ -OV	276	3.43
TiO ₂	224	3.42

Table S2. Determined AQEs for Ammonia Production at Different Wavelengths

wavelength (nm)	ammonia produced ($\mu\text{mol h}^{-1}$)	light power density I (mW cm^{-2})	light power P (mW)	AQE (%)
420	1.28	3.45	55.48	0.55
475	1.58	3.69	59.34	0.56
520	2.04	3.69	59.34	0.66
550	2.64	3.63	58.37	0.82
600	1.91	3.79	60.94	0.52
650	1.01	3.84	61.75	0.25
700	0.54	3.66	58.85	0.13

The reactor was irradiated with light from the side. The projected area of the reactor on the side in the direction of the light irradiation was circular with a diameter of 6.4 cm. The reaction solution occupied one half of the capacity of the reactor. Therefore, the irradiated area, S , of the reaction solution is

$$S = \frac{\pi \times 3.2^2}{2} = 16.08 \text{ cm}^2$$

Take the estimation of the AQE at 550 nm as an example.

The light power is

$$P = IS = 3.63 \times 16.08 = 58.37 \text{ mW}$$

The number of the incident photons is

$$N_{\text{incident}} = \frac{Pt}{h\nu} = \frac{Pt\lambda}{hc} = \frac{58.37 \times 10^{-3} \times 3600 \times 550 \times 10^{-9}}{6.63 \times 10^{-34} \times 3 \times 10^8} = 5.81 \times 10^{20}$$

In the equation above, t is the time (1 h = 3600 s), h is Planck's constant, ν is the light frequency, and c is the speed of light in free space.

The number of the reacted electrons is

$$\begin{aligned} N_{\text{reacted}} &= 3 \times \text{the number of the produced ammonia molecules} \\ &= 3 \times 2.64 \times 10^{-6} \times 6.02 \times 10^{23} = 4.77 \times 10^{18} \end{aligned}$$

The AQE can then be calculated as

$$\text{AQE} = \frac{N_{\text{reacted}}}{N_{\text{incident}}} \times 100\% = \frac{4.77 \times 10^{18}}{5.81 \times 10^{20}} \times 100\% = 0.82\%$$

Table S3. Representative Works on Photocatalytic N₂ Fixation

catalyst	light source	condition	NH ₃ production rate	AQE	ref.
TiO ₂ -OV	300 W Hg lamp, $\lambda > 280$ nm	200 mL water, 200 mg catalyst, 40 °C	0.73 $\mu\text{mol/h/g}$	0.7% at $\lambda < 350$ nm	3
Bi ₅ O ₇ Br-OV	300 W Xe lamp, $\lambda > 400$ nm	100 mL water, 25 mg catalyst, ambient temperature	1.38 mmol/h/g	2.3% at 420 nm	4
CuCr	300 W Xe lamp, $\lambda > 400$ nm	20 mL water, 50 mg catalyst, 25 °C	73.9 $\mu\text{mol/h/g}$	0.10% at 500 nm	5
Diamond	450 W high- pressure Hg/Xe lamp, $\lambda > 190$ nm	35 mL water, 11.6 mg KI, 35 mg catalyst, ambient temperature	7.43 $\mu\text{mol/h/g}$	0.6% at 211.5 nm, 0.15% at 223.5 nm	6
CdS:MoFe protein	405 nm diode light source at 25 mW/cm ²	300 μL solution of 16.7 nM CdS and MoFe protein, 500 mM HEPES, 25 °C	18.9 $\mu\text{mol/h/(mg of}$ MoFe protein)	0.33% at 405 nm	7
BiOBr-OV	300 W Xe lamp, $\lambda > 420$ nm	100 mL water, 50 mg catalyst, 25 °C	104.2 $\mu\text{mol/h/g}$	0.23% at 420 nm	8
FeS-SnS chalcogel	150 W Xe lamp, $\lambda > 190$ nm	10 mL water, 150 mg wet chalcogel, room temperature	1.2 $\mu\text{mol/h/(g}$ wet chalcogel)		9
Fe@3D graphene	500 W high- pressure Hg lamp, full spectrum	Gas reactor of 944 mL in capacity, 240 mg catalyst, flowing H ₂ /N ₂ (3/1, v/v), 200 \pm 10 °C	24 $\mu\text{mol/h/g}$		10
Fe-doped TiO ₂	360 W Hg arc lamp, full spectrum	38 mL water, 200 mg catalyst, 40 \pm 5 °C	11.58 $\mu\text{mol/h/g}$		11
C-WO ₃ -H ₂ O	500 mW/cm ² Xe lamp, visible light	150 mL water, 50 mg catalyst, 25 °C	63.55 $\mu\text{mol/h/g}$		12
Ru/TiO ₂	150 W Xe arc lamp, full spectrum	19 mL water, 1 mL methanol, 100 mg catalyst, 25 °C	29.4 $\mu\text{mol/h/g}$		13
Pt-CdS	100 W high- pressure Hg lamp, full spectrum	270 mL water, 300 mg catalyst, 38 °C	16.3 $\mu\text{mol/h/g}$		14

Fe ₂ O ₃	150 W Xe lamp, full spectrum	30 mL water, 30 mg catalyst, 29–30 °C	10.0 μmol/h/g		15
Au/TiO ₂ -OV	300 W Xe lamp, λ > 420 nm	72 mL water, 8 mL methanol, 100 mg catalyst, 25 °C	130.5 μmol/h/g	0.82% at 550 nm	This work

Table S4. Flat-Band Potentials and Apparent Electron Carrier Concentrations of the Different Catalysts

catalyst	flat-band potential E_{fb} (V, vs Ag/AgCl)	apparent electron carrier concentration n (cm ⁻³)
Au/TiO ₂ -OV	-1.05	3.63×10^{21}
Au/TiO ₂	-1.07	5.64×10^{20}
TiO ₂ -OV	-1.06	1.71×10^{21}
TiO ₂	-1.08	2.89×10^{20}

As shown in Figure 4d, E_{fb} and n were calculated from the Mott-Schottky plots according to the following relationship¹⁶

$$\frac{1}{C^2} = \frac{2}{eA^2\epsilon_r\epsilon_0n} \left(E - E_{fb} - \frac{kT}{e} \right)$$

where C is the interfacial capacitance between the semiconductor and the electrolyte, A is the interfacial area (1 cm²), e is the electron charge, ϵ_0 is the vacuum permittivity, ϵ_r is the relative permittivity of anatase TiO₂ at 1 kHz frequency.¹⁷ n is the apparent electron carrier concentration, E is the applied voltage, E_{fb} is the flat-band potential, k is the Boltzmann constant, and T is the absolute temperature. A plot of A^2/C^2 against E gives a straight line from which E_{fb} can be determined from the intercept on the E axis and the electron carrier concentration n can be calculated from the slop of the straight line.

Take Au/TiO₂-OV as an example.

The slope of the straight line obtained from Figure 4d is 1.44×10^9 cm⁴ F⁻² V⁻¹. We then have

$$\frac{2}{e\epsilon_r\epsilon_0n} = 1.44 \times 10^9$$

Therefore, we obtain

$$n = \frac{2}{1.44 \times 10^9 \times 1.6 \times 10^{-19} \times 27 \times 8.854 \times 10^{-14}} = 3.63 \times 10^{21} (\text{cm}^{-3})$$

Supporting References

- (1) Tauc, J.; Grigorovici, R.; Vancu, A. Optical Properties and Electronic Structure of Amorphous Germanium. *Phys. Stat. Sol.* **1966**, *15*, 627–637.
- (2) Kavan, L.; Grätzel, M.; Gilbert, S. E.; Klemenz, C.; Scheel, H. J. Electrochemical and Photoelectrochemical Investigation of Single-Crystal Anatase. *J. Am. Chem. Soc.* **1996**, *118*, 6716–6723.
- (3) Hirakawa, H.; Hashimoto, M.; Shiraishi, Y.; Hirai, T. Photocatalytic Conversion of Nitrogen to Ammonia with Water on Surface Oxygen Vacancies of Titanium Dioxide. *J. Am. Chem. Soc.* **2017**, *139*, 10929–10936.
- (4) Wang, S. Y.; Hai, X.; Ding, X.; Chang, K.; Xiang, Y. G.; Meng, X. G.; Yang, Z. X.; Chen, H.; Ye, J. H. Light-Switchable Oxygen Vacancies in Ultrafine Bi₅O₇Br Nanotubes for Boosting Solar-Driven Nitrogen Fixation in Pure Water. *Adv. Mater.* **2017**, *29*, 1701774.
- (5) Zhao, Y. F.; Zhao, Y. Z. X.; Waterhouse, G. I. N.; Zheng, L. R.; Cao, X. Z.; Teng, F.; Wu, L.-Z.; Tung, C.-H.; Hare, D. O.; Zhang, T. R. Layered-Double-Hydroxide Nanosheets as Efficient Visible-Light-Driven Photocatalysts for Dinitrogen Fixation. *Adv. Mater.* **2017**, *29*, 1703828.
- (6) Zhu, D.; Zhang, L. H.; Ruther, R. E.; Hamers, R. J. Photo-Illuminated Diamond as a Solid-State Source of Solvated Electrons in Water for Nitrogen Reduction. *Nat. Mater.* **2013**, *12*, 836–841.
- (7) Brown, K. A.; Harris, D. F.; Wilker, M. B.; Rasmussen, A.; Khadka, N.; Hamby, H.; Keable, S.; Dukovic, G.; Peters, J. W.; Seefeldt, L. C.; King, P. W. Light-Driven Dinitrogen Reduction Catalyzed by a CdS:Nitrogenase MoFe Protein Biohybrid. *Science* **2016**, *352*, 448–450.
- (8) Li, H.; Shang, J.; Ai, Z. H.; Zhang, L. Z. Efficient Visible Light Nitrogen Fixation with BiOBr Nanosheets of Oxygen Vacancies on the Exposed {001} Facets. *J. Am. Chem. Soc.* **2015**, *137*, 6393–6399.

- (9) Liu, J.; Kelley, M. S.; Wu, W. Q.; Banerjee, A.; Douvalis, A. P.; Wu, J. S.; Zhang, Y. B.; Schatz, G. C.; Kanatzidis, M. G. Nitrogenase-Mimic Iron-Containing Chalcogels for Photochemical Reduction of Dinitrogen to Ammonia. *Proc. Natl. Acad. Sci. USA* **2016**, *113*, 5530–5535.
- (10) Lu, Y. H.; Yang, Y.; Zhang, T. F.; Ge, Z.; Chang, H. C.; Xiao, P. S.; Xie, Y. Y.; Hua, L.; Li, Q. Y.; Li, H. Y.; Ma, B.; Guan, N. J.; Ma, Y. F.; Chen, Y. S. Photoprompted Hot Electrons from Bulk Cross-Linked Graphene Materials and their Efficient Catalysis for Atmospheric Ammonia Synthesis. *ACS Nano* **2016**, *10*, 10507–10515.
- (11) Schrauzer, G. N.; Guth, T. D. Photolysis of Water and Photoreduction of Nitrogen on Titanium Dioxide. *J. Am. Chem. Soc.* **1977**, *99*, 7189–7193.
- (12) Li, X. M.; Wang, W. Z.; Jiang, D.; Sun, S. M.; Zhang, L.; Sun, X. Efficient Solar-Driven Nitrogen Fixation over Carbon–Tungstic-Acid Hybrids. *Chem. Eur. J.* **2016**, *22*, 13819–13822.
- (13) Ranjit, K. T.; Varadarajan, T. K.; Viswanathan, B. Photocatalytic Reduction of Dinitrogen to Ammonia over Noble-Metal-Loaded TiO₂. *J. Photochem. Photobiol. A: Chem.* **1996**, *96*, 181–185.
- (14) Miyama, H.; Fujii, N.; Nagae, Y. Heterogeneous Photocatalytic Synthesis of Ammonia from Water and Nitrogen. *Chem. Phys. Lett.* **1980**, *74*, 523–524.
- (15) Khader, M. M.; Lichtin, N. N.; Vurens, G. H.; Salmeron, M.; Somorjai, G. A. Photoassisted Catalytic Dissociation of H₂O and Reduction of N₂ to NH₃ on Partially Reduced Fe₂O₃. *Langmuir* **1987**, *3*, 303–304.
- (16) Spagnol, V.; Sutter, E.; Debiemme-Chouvy, C.; Cachet, H.; Baroux, B. EIS Study of Photo-Induced Modifications of Nano-Columnar TiO₂ Films. *Electrochim. Acta* **2009**, *54*, 1228–1232.
- (17) Kalaiarasi, S.; Jose, M. Dielectric Functionalities of Anatase Phase Titanium Dioxide Nanocrystals Synthesized Using Water-Soluble Complexes. *Appl. Phys. A* **2017**, *123*, 512.